Publised online in Earthquake Engineering and Structural Dynamics
Citation: Akkar S and Cheng Y (2015). Application of Monte-Carlo simulation approach for the probabilistic assessment of seismic hazard for geographically distributed portfolio, *Earthqauke Engineering and Structural Dynamics* (published online in Wiley online library, doi: 10.1002/eqe.2667)

Application of a Monte-Carlo simulation approach for the probabilistic assessment of seismic hazard for geographically distributed portfolio

Sinan Akkar and Yin Cheng

Earthquake Engineering Department, Boğaziçi University Kandilli Observatory and Earthquake Research Institute, 34684 Çengelköy İstanbul

SUMMARY

The conventional integral approach is very well established in probabilistic seismic hazard assessment (PSHA). However, Monte-Carlo (MC) simulations can become an efficient and flexible alternative against conventional PSHA when more complicated factors (e.g., spatial correlation of ground shaking) are involved. This study aims at showing the implementation of MC simulation techniques for computing the annual exceedance rates of dynamic ground-motion intensity measures (GMIMs) (e.g., peak ground acceleration, PGA and spectral acceleration, S_a). We use multi-scale random fields (MSRFs) technique to incorporate spatial correlation and near-fault directivity while generating MC simulations to assess the probabilistic seismic hazard of dynamic GMIMs. Our approach is capable of producing conditional hazard curves as well. We show various examples to illustrate the potential use of the proposed procedures in the hazard and risk assessment of geographically distributed structural systems.

1. INTRODUCTION

The consideration of site-to-site variation (spatial correlation) in dynamic GMIMs (e.g., PGA, S_a) is important for realistic probabilistic seismic hazard and risk assessment of geographically distributed building portfolios and lifeline systems. The interdependency between the GMIMs (cross-correlation) is also important for such structural systems because some of their components are vulnerable to the conditional occurrence of multiple GMIMs. Apart from these considerations, the proper amplitude estimations of dynamic GMIMs is crucial for geographically distributed buildings or lifelines located in the close proximity to fault segments.

Studies to model spatial correlation (e.g., [1-6]), cross-correlation (e.g., [7-14]), combined effects of spatial- and cross-correlation (e.g., [3, 15]) as well as near-fault effects on dynamic GMIMs ([16-21]) are abundant in the literature. There are also several papers showing their implementation by using conventional PSHA [22] (e.g., [18, 23–25]). Alternative to conventional PSHA, Monte Carlo (MC) simulation techniques have become appealing in probabilistic hazard calculations as they provide flexibility, transparency and robustness [26] while considering the above complex features in earthquake phenomenon (e.g., [27–29]). Monte Carlo simulations are also used in probabilistic risk assessment of geographically distributed systems (e.g., [26, 30–33]). Crowley and Bommer [26] demonstrated that the use of MC simulations leads to lesser conservatism with respect to conventional probabilistic risk

assessment at multiple sites as they could easily adopt the spatial correlation in GMIMs. Sokolov and Wenzel [30, 31] used MC simulations to emphasize the significance of proper modeling in between-earthquake and site-to-site (spatial) correlations for seismic loss estimation of distributed portfolios. Based on MC simulations, Jayaram and Baker [34] proposed an efficient simulation-based framework for developing a small but stochastically representative catalog of earthquake ground-motion intensity maps that can be used for lifeline risk assessment. Wang et al. [35] used MC simulations to assess the seismic risk of the water supply systems by identifying the most critical links that would affect their seismic performance. In a similar manner, Esposito et al. [36] assessed the performance of gas distribution network of the L'Aquila city both for dynamic GMIMs and fault displacements by applying MC simulations. Recently, Weatherill et al. [37] explored the effect of spatially cross-correlated random fields of different GMIMs on seismic risk analysis for the Tuscany region in Italy.

This study implements MC simulation technique together with the multi-scale random fields (MSRFs) approach [38] to account for spatial correlation in estimating the joint hazard of dynamic GMIMs for geographically distributed structural systems. The proposed approach differs from other MC-based seismic hazard procedures that generate normally distributed and spatially correlated GMIMs via Cholesky decomposition (e.g., [37]). As indicated above we propagate its application into PSHA as an alternative to Cholesky decomposition technique. At the expense of increased computational burden (which is the case in all MC-based methods), MSRFs technique can account for spatial correlation at different precision levels in order to fine-tune the accuracy of hazard curves at the mesh grids critical to design and risk assessment of geographically distributed structures. Using particular properties of MSRFs technique and flexibility provided by MC simulations, we further implemented the near-fault directivity effects on the hazard computations. The paper first describes the PSHA of dynamic GMIMs through the application of MC-based MSRFs approach. This part is followed by demonstrating several examples to discuss the strengths of the proposed procedures for the hazard assessment of geographically distributed building portfolios and lifeline systems.

2. MONTE-CARLO BASED MULTI-SCALE RANDOM FIELDS FOR DYNAMIC GMIMs

The multi-scale random fields (MSRFs) hierarchically characterize the randomness of a physical process at different resolution levels. We use this concept together with MC simulations to generate spatially correlated intra-event residuals by following Chen Q et al. [38] who studied the mechanical behavior of heterogeneous soil medium under different levels of uncertainty. The spatially correlated intra-event residuals leads to the sampling of spatially correlated GMIMs over the region of interest. MSRFs method is based on regular grids of cells. The residuals as well as the GMIMs are sampled at the centroids of the cells. Therefore, the separation distances used in the spatial correlations are centroidal distances. The sampled GMIMs can account for near-fault directivity effects depending on the relative locations of the sites with respect to the fault. Our procedure also considers cross-correlation of sampled primary and secondary GMIMs to assess conditional hazard.

We implement two scale levels (coarse-scale and fine-scale) while generating spatially correlated intra-event residuals. Figure 1 illustrates the coarse-scale and fine-scale random fields (coarse-scale and fine-scale cells). The center-to-center distances between the cells are used in spatial correlation as the sampled residuals are located at the mid points of the grids. The sampled intra-event residual in a coarse-scale cell is the average of sampled intra-event

residuals of fine-scale cells within the corresponding coarse-scale cell. This relationship is given in Equation 1 where *Z* stands for the sampled intra-event residual. The indices "*1*" and "*2*" designate coarse-scale and fine-scale cells, respectively. *n* is the number of fine-scale cells within the coarse-scale cell and *b* represents the index number of the coarse-scale cell.

$$Z_{1,b} = \frac{1}{n}\sum_{i=1}^{n} Z_{2,bi} \tag{1}$$

The intra-event residuals are sampled via MC simulation and we make use of the intra-event standard deviation of the GMPE used in the entire process. The intra-event standard deviation accounts for the variability in sampled intra-event residuals. Spatial correlation is considered while sampling the intra-event residuals to mimic the interdependency of generated GMIMs at closely spaced sites (cells) because the waveform radiation patterns are coherent at close sites under a given earthquake. The intra-event residual sampling starts from coarse-scale fields and extends into fine-scale as well as coarse-to-fine scale cells through sequential conditional simulation. The sequential conditional simulation transfers the knowledge of previously sampled intra-event residuals to the next sampled intra-event residual.

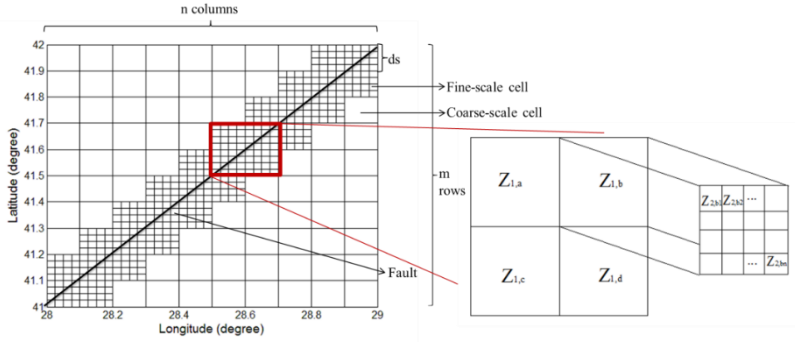

Figure 1. Graphical representation of coarse-scale and fine scale cells. The solid diagonal line is the fault. The area enclosing the fault segment is divided into *m*×*n* coarse-scale cells. Some of the coarse-scale cells are further refined into *ds*×*ds* fine scale cells. The right panel is the close-up view of 4 coarse scale cells located in the vicinity of the fault and, for illustration purposes, we show one of these coarse scale cells refined into 4×4 fine-scale cells

Although MC-based intra-event residual sampling starts at coarse-scale level, the sampling distributions of coarse-scale and fine-scale cells are directly related to each other. The intra-event residual distribution at fine-scale level is normal with zero mean and standard deviation σ_{Z2}. σ_{Z2} is the intra-event standard deviation of the pertaining GMPE used in the calculations. Equation (1) leads to the below expressions to compute the mean (μ_{Z1}) and standard deviation (σ_{Z1}) of normally distributed intra-event residuals for coarse-scale cells.

$$\mu_{Z1} = E(Z_1) = E(\frac{1}{n}\sum_{i=1}^{n} Z_{2i}) = \frac{1}{n}E(\sum_{i=1}^{n} Z_{2i}) = \frac{1}{n}\sum_{i=1}^{n} E[Z_{2i}] = 0 \tag{2}$$

$$\sigma_{Z1}^2 = E[Z_1^2] - E[Z_1]^2 = E[Z_1^2] - 0 = \frac{1}{n^2}\sum_{i=1}^{n}\sum_{j=1}^{n} \rho_{Z2i,Z2j} \cdot \sigma_{Z2i} \cdot \sigma_{Z2j} \tag{3}$$

In Equation (3), $\rho_{Z2i,Z2j}$ is the spatial correlation coefficient between two fine-scale cells that is controlled by the separation distance between them. As discussed in the introduction, there are handful spatial correlation models in the literature for calculating $\rho_{Z2i,Z2j}$ (e.g.,[3]). σ_{Z2i} and σ_{Z2j}

are the intra-event residual standard deviations of the *ith* and *jth* fine-scale cells, respectively. *Z* is the sampled intra-event residual, *n* is the number of fine-scale cells in the corresponding coarse-scale cell and indices *1* and *2* indicate coarse-scale and fine-scale cells, respectively. *E* denotes the expected value operator. The spatial correlation coefficient between two fine-scale cells, $\rho_{Z2i,Z2j}$, is used to derive spatial correlation coefficients for coarse-to-coarse scale and coarse-to-fine scale cells. These expressions are given in Equations (4) and (5) and are used to sample intra-event residuals by sequential conditional simulation.

$$\begin{aligned}\rho_{Z1a,Z1b} &= \frac{\mathrm{cov}[Z_{1a}, Z_{1b}]}{\sigma_{Z1a}\sigma_{Z1b}} \\ &= \frac{\mathrm{cov}[1/n\sum_{i=1}^{n} Z_{2ai}, 1/n\sum_{k=1}^{n} Z_{2bk}]}{\sqrt{1/n^2\sum_{i=1}^{n}\sum_{j=1}^{n}\rho_{Z2ai,Z2aj}\cdot\sigma_{Z2ai}\cdot\sigma_{Z2aj}}\sqrt{1/n^2\sum_{i=1}^{n}\sum_{j=1}^{n}\rho_{Z2bi,Z2bj}\cdot\sigma_{Z2bi}\cdot\sigma_{Z2bj}}} \\ &= \frac{\sum_{i=1}^{n}\sum_{k=1}^{n}\mathrm{cov}(Z_{2bi}, Z_{2ak})}{\sqrt{\sum_{i=1}^{n}\sum_{j=1}^{n}\rho_{Z2ai,Z2aj}\cdot\sigma_{Z2ai}\cdot\sigma_{Z2aj}}\cdot\sqrt{\sum_{i=1}^{n}\sum_{j=1}^{n}\rho_{Z2bi,Z2bj}\cdot\sigma_{Z2bi}\cdot\sigma_{Z2bj}}} \\ &= \frac{\sum_{i=1}^{n}\sum_{k=1}^{n}\rho_{z_{2ai},z_{2bk}}\cdot\sigma_{z_{2ai}}\cdot\sigma_{z_{2bk}}}{\sqrt{\sum_{i=1}^{n}\sum_{j=1}^{n}\rho_{Z2ai,Z2aj}\cdot\sigma_{Z2ai}\cdot\sigma_{Z2aj}}\cdot\sqrt{\sum_{i=1}^{n}\sum_{j=1}^{n}\rho_{Z2bi,Z2bj}\cdot\sigma_{Z2bi}\cdot\sigma_{Z2bj}}}\end{aligned} \tag{4}$$

$$\begin{aligned}\rho_{Z2,Z1a} &= \frac{\mathrm{cov}[Z_2, Z_{1a}]}{\sigma_{Z2}\sigma_{Z1a}} = \frac{\mathrm{cov}[Z_2, 1/n\sum_{i=1}^{n} Z_{2ai}]}{\sigma_{Z2}\sqrt{1/n^2\sum_{i=1}^{n}\sum_{j=1}^{n}\rho_{Z2ai,Z2aj}\cdot\sigma_{Z2ai}\cdot\sigma_{Z2aj}}} \\ &= \frac{\sum_{i=1}^{n}\mathrm{cov}(Z_2, Z_{2ai})}{\sigma_{Z2}\sqrt{\sum_{i=1}^{n}\sum_{j=1}^{n}\rho_{Z2ai,Z2aj}\cdot\sigma_{Z2ai}\cdot\sigma_{Z2aj}}} = \frac{\sum_{i=1}^{n}\rho_{Z2,Z2ai}\cdot\sigma_{Z2ai}}{\sqrt{\sum_{i=1}^{n}\sum_{j=1}^{n}\rho_{Z2ai,Z2aj}\cdot\sigma_{Z2ai}\cdot\sigma_{Z2aj}}}\end{aligned} \tag{5}$$

In the above expressions, $\rho_{Z1a,Z1b}$ and $\rho_{Z2,Z1a}$ refer to coarse-to-coarse scale and fine-to-coarse scale correlation coefficients, respectively. The parameters *a* and *b* indicate the index numbers of coarse-scale cells. Equation (6) shows the joint distribution expression used in the spatially correlated intra-event sampling by conditional sequential simulation.

$$\begin{bmatrix} Z_n \\ \boldsymbol{Z}_p \end{bmatrix} \sim N(\boldsymbol{\mu}, \boldsymbol{\Sigma}) = N\left(\begin{bmatrix} 0 \\ \mathbf{0} \end{bmatrix}, \begin{bmatrix} \sigma_n^2 & \boldsymbol{\Sigma}_{np} \\ \boldsymbol{\Sigma}_{pn} & \boldsymbol{\Sigma}_{pp} \end{bmatrix}\right) \tag{6}$$

The subscripts *n* and *p* describe the "next" and "previously" generated intra-event residuals, respectively in Equation (6). The vector $\boldsymbol{Z}=[Z_n\ \boldsymbol{Z_p}]$ follows a joint normal distribution with a vector of zero mean and covariance matrix, $\sum$. The distribution of the next sampled data (Z_n) is a univariate normal distribution conditioned on the previously sampled realizations ($\boldsymbol{Z_p}$) that is given in Equations (7) and (8).

$$\left[Z_n \mid \boldsymbol{Z}_p = \boldsymbol{z} \right] \sim N\left(\boldsymbol{\Sigma}_{np}\cdot\boldsymbol{\Sigma}_{pp}^{-1}\cdot\mathbf{z}, \sigma^2 - \boldsymbol{\Sigma}_{np}\cdot\boldsymbol{\Sigma}_{pp}^{-1}\cdot\boldsymbol{\Sigma}_{pn}\right) \tag{7}$$

$$\mathrm{COV}\left[Z_i, Z_j \right] = \rho_{Z_i,Z_j}\cdot\sigma_{Z_i}\cdot\sigma_{Z_j} \tag{8}$$

While sampling the intra-event residuals of coarse-scale cells, the covariance matrix ($\sum$) given in Equation (8) considers the spatial correlation between two coarse-scale cells as shown in Equation (4). The corresponding intra-event standard deviations σ_{Zi} and σ_{Zj} can be calculated from Equation (3). If the intra-event residual sampling is for fine-scale cells, the covariance matrix considers the spatial correlation between two fine-scale cells ($\rho_{Z2i,Z2j}$), two coarse-scale cells (Equation 4) as well as one coarse-scale cell and one fine-scale cell (Equation 5).

Accordingly, the intra-event standard deviations in Eq. (8) would correspond to one of these three cases for the intra-event residual sampling of fine scale cells. These concepts are further clarified in the following paragraphs.

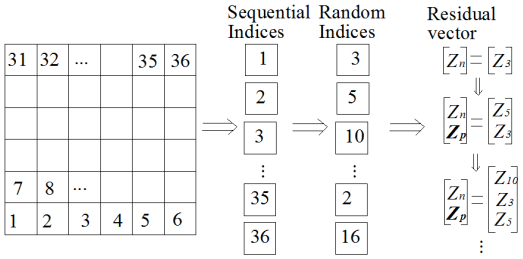

Figure 2. Illustrative example for intra-event residual sampling at coarse-scale level

Figure 2 illustrates the generation of intra-event residuals at coarse-scale level. The area of interest is divided into a number of coarse-scale cells and indexed from left-to-right and bottom-to-top as given in the leftmost side of Figure 2. The sequential indices are resorted in a random manner to generate a new sequence of indices (middle part in Figure 2). Following the new order of randomized coarse-scale cells, the intra-event residuals are generated for each cell at the coarse-scale level by using the sequential conditional simulation procedure as summarized in Equations (6), (7) and (8). The intra-event residual of first coarse-scale cell (Z_3 in the illustrative example as given in the rightmost part in Figure 2) is sampled as a univariate normal distribution. The intra-event residual of coarse-scale cell following the first one (Z_5 in Figure 2) is sampled by using the sampled intra-event residual of first coarse-cell (Z_3). In essence, while generating the intra-event residual of the "next" cell, Z_n, the previously generated intra-event residuals become the entries in $\boldsymbol{Z_p}$. The procedure is recursively repeated until all the intra-event residuals in the coarse-scale cells are sampled.

The intra-event residual simulation of coarse-scale cells is followed by a similar set of simulations at fine-scale level. This process is illustrated in Figure 3 as the continuation of the example case in Figure 2. Although the entire coarse-scale cells can be refined into fine-scale cells to generate the intra-event residuals at the fine-scale level, this process may bring computational burden depending on the size of the area of interest, the number of coarse-scale cells as well as the level of mesh gridding at the fine-scale level (i.e., the number of fine-scale cells in coarse-scale cells). We prefer pre-defining the coarse-scale cells to be refined into fine-scale cells in our procedure. The level of precision in observing the near-fault effects on hazard computations or requirements to be fulfilled in the development of conditional hazard curves can play a role on the number of pre-defined coarse-scale cells for fine-scale mesh gridding. The order of coarse-scale cells to be refined into fine-scale cells should follow the random indexing used while generating the intra-event residuals of coarse-scale cells. In the follow-up example given in Figure 3, the coarse-scale cells indexed as #2 and #3 are chosen to be refined into fine-scale cells (Figure 3.a). Note that the random coarse-scale cell indexing given in Figure 2 indicates that conditional sequential simulation for fine-scale cells should start from coarse-scale cell #3 and should be followed by refining the coarse-scale cell #2. Similar to the indexing technique given in Figure 2, the fine-scale cells in the #2 and #3 coarse-scale cells are numbered from left-to-right and from bottom-to-top as shown in Figure 3.a. For this illustrative case, each coarse-scale cell is mesh gridded into 2×2 fine-scale cells. The fine-scale cell indices are then randomized (leftmost part in Figure 3.b) to start sequential conditional simulation. For example, the randomized indices of fine-scale cells in the #3 coarse-scale cell are [4, 2, 3, 1].

As presented in the illustrative case in Figure 3, the intra-event residual of the #4 fine-scale cell in the #3 coarse-scale cell ($Z_{3,4}$) is sampled by using Equations (6) to (8) where $\boldsymbol{Z_p}$ contains all previously sampled coarse-scale cell intra-event residuals. The intra-event residual sampling $Z_{3,2}$, $Z_{3,3}$ and $Z_{3,1}$ is followed after $Z_{3,4}$. After each realization, the corresponding sampled intra-event residual is an entry in $\boldsymbol{Z_p}$. Upon the sampling of all intra-event residuals in the fine-scale cells of a coarse-scale cell (e.g., #3 coarse-scale cell in Figure 3), it is removed from the previously sampled realizations vector, $\boldsymbol{Z_p}$. The entire process is repeated until the sampling of all intra-event residuals at fine-scale level is finished in the pre-defined coarse-scale random fields. The following section extends our approach to include near-fault forward directivity effects on the spatially correlated dynamic GMIMs generated via MC-based MSRFs approach.

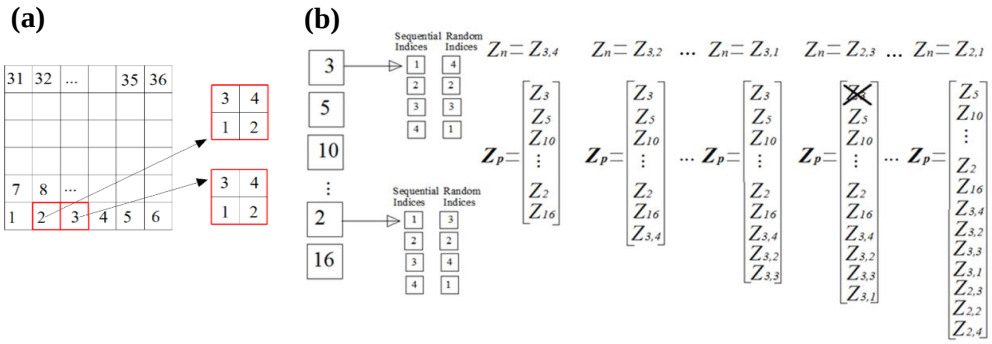

Figure 3. Generation of intra-event residuals for fine-scale cells: (a) pre-selected coarse-scale cells for refining into fine-scale cells (designated by red boxes) and numbering of fine-scale cells in these coarse-scale cells, (b) sequential conditional simulation process

We note that the MSRFs approach sample the spatially correlated residuals and GMIMs at the centroids of the grids. Therefore, the computation of GMIMs at locations within the grids require additional computational effort and assumptions. One can assume that the central GMIMs apply uniformly within the grids that imply a perfect spatial correlation within the cell. The accuracy of hazard computed under this assumption is related to the grid size: smaller grid sizes would increase the accuracy of hazard at sites far from the centroids of the grids. Smaller grids would also allow the expert to use a proper interpolation method (inverse distance weighting, krigging, etc.) to interpolate the central GMIMs for other sites within the grids. Alternatively, one can use grid-to-grid correlation and grid variance [39] instead of point-to-point correlation or GMPE variance as presented in Equations (3) to (5). Our analysis from the implementation of Stafford's [39] grid variance expression indicate that a grid size of 1km × 1km would yield almost equal point and grid variances. Thus, the use of such a grid dimension for the computation of central hazard in a cell would resemble the hazard for sites anywhere within that cell. Needless to say these alternative methods to estimate GMIM distribution at sites other than the centers of the cells would increase the computational burden that is also valid for any MC-based probabilistic hazard assessment method. In their paper, Bal et al. [33] discuss the trade-offs between grid size, hazard accuracy and computer time that highlight important points for an efficient and accurate computation in MC-based hazard studies. The case studies in this paper only consider the hazard computed at the center of the cells.

2.1 Near-fault directivity effects

When the rupture and slip direction relative to a site coincide and a significant portion of the fault ruptures towards the site, the ground motion can exhibit the effects of forward directivity

(short duration ground motions that consist of one or more pulses). Most of the conventional GMPEs do not model forward directivity so seismic hazard assessment via conventional ground-motion characterization may fail to estimate the near-fault ground-motion amplitudes for future earthquakes. We implemented the near-fault directivity model of Shahi and Baker [18] to account for the likely change of ground-motion amplitudes in the vicinity of faults. The Shahi and Baker model predicts the probability of pulse-like ground motions occurring at a site by considering the orientations of induced seismic waveforms relative to the strike of the fault. It amplifies the spectral ordinates in the vicinity of pulse period, T_p, by empirically calibrating the median and standard deviations of ground-motion estimates from conventional GMPEs. Strictly speaking the Shahi and Baker [18] model requires a spatial correlation function that is explicitly developed for near-fault effects. The use of a spatial correlation function that disregards near-fault effects may mask the actual spatial distribution of ground motion in the vicinity of the fault. To our knowledge, there is no such spatial correlation function that explicitly accounts for the near-fault effects. The reader should consider this fact while implementing the proposed approach for the assessment of hazard in the close proximity of faults.

Figure 4 shows the overall algorithm for incorporating the near-fault directivity effects to the spatially correlated GMIMs generated via MSRFs approach. In essence, we modify the intra-event standard deviation of the conventional GMPE to sample the spatially correlated intra-event residuals for sites (coarse and fine-scale cells) located in the near-fault region. Considering T_p, we also modify the median estimates of GMIMs for these sites obtained from the conventional GMPE. For each realization of MC simulations (i.e., for each scenario event), we determine the probability of observing a pulse at a certain orientation α [P(pulse at α|pulse)] for the mid-point of the cells that are located in the vicinity of fault. P(pulse at α|pulse) is related to the relative location of the centroid of the cell with respect to the fault strike. We sample this value using binomial distribution. If the forward directivity is more likely to occur (Pulse case), we sample T_p assuming log-normal distribution. The value of sampled T_p leads to the calibration of median ground motion and associated standard deviation of conventional GMPE to generate spatially correlated random fields. The Shahi and Baker [18] model disregards the calibration of median ground motion and associated standard deviation if $T_p < 0.6$s. If no pulse case is dominant, then depending on the spectral period (T) of GMIM, this model either uses the median ground-motion estimates and standard deviation of conventional GMPE ($T \leq 1.0$s case) or modifies these parameters. The calibrated standard deviations and median ground-motion estimates are used for generating spatially correlated GMIMs at coarse- and fine-scale levels. As the MSRFs method considers the centers of the cells for sampling GMIMs, the distribution of GMIMs due to near-fault effects would be more accurate with smaller grid sizes at the expense of increased computational burden.

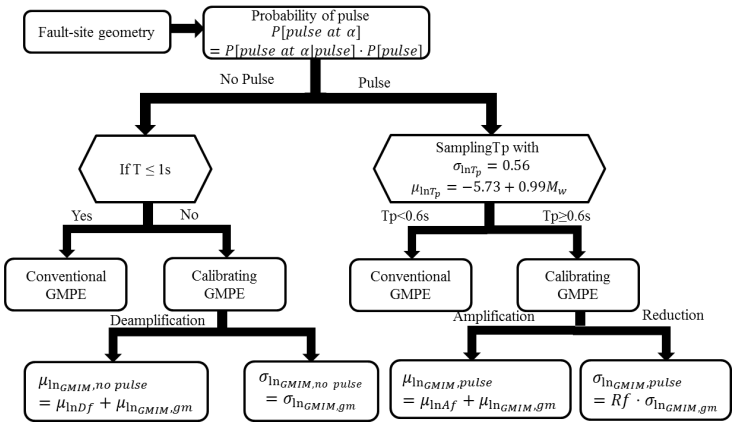

Figure 4. Algorithm for considering near-fault forward directivity effects on the spatially correlated GMIMs generated from MSRFs approach. $\mu_{lnGMIM,pulse}$ is the calibrated mean GMIM in logarithmic space due to pulse-like ground motions (forward directivity). μ_{lnAF} is the logarithmic calibration factor for forward directivity effects and $\mu_{lnGMIM,gm}$ is the mean GMIM in logarithmic space computed from conventional GMPE. In a similar manner, $\sigma_{lnGMIM,pulse}$ and $\sigma_{lnGMIM,gm}$ are the calibrated and original standard deviations of conventional GMPE, respectively. Rf is the calibration factor for standard deviation for forward directivity effects. For non-pulse case, $\mu_{lnGMIM,nonpulse}$ is the calibrated mean GMIM in logarithmic space due to non-pulse-like ground motions. μ_{lnAF} and $\sigma_{lnGMIM,nonpulse}$ are the logarithmic calibration factor and standard deviation of GMPE for backward directivity effects, respectively.

The Shahi and Baker model provides calibration factors for the total standard deviation of a conventional GMPE that can be used for generating total residuals. Since the MSRFs approach requires intra-event standard deviation ($\sigma_{\varepsilon,gm}$) to sample intra-event residuals, we modify the calibration factor proposed in Shahi and Baker as given in Equations (9) and (10). We assume that the inter-event standard deviation ($\sigma_{\eta,gm}$) does not change for any given simulated scenario earthquake. This assumption is rational as inter-event standard deviation is constant for a specific earthquake. The modified calibration factor is indicated as $Rf_{\varepsilon,\ pulse}$ in the derivations and replaces R_f (see the last row of "Pulse" case in Figure 4) while considering the near-fault directivity effects in the MSRFs approach. Note that $\sigma_{\eta,gm}$ and $\sigma_{\eta,pulse}$ are equal to each other in the derivations under constant inter-event standard deviation assumption.

$$Rf^2 = \frac{\sigma_{t,pulse}^2}{\sigma_{t,gm}^2} = \frac{\sigma_{\varepsilon,pulse}^2 + \sigma_{\eta,pulse}^2}{\sigma_{\varepsilon,gm}^2 + \sigma_{\eta,gm}^2} = \frac{\sigma_{\varepsilon,pulse}^2 / \sigma_{\varepsilon,gm}^2 + \sigma_{\eta,pulse}^2 / \sigma_{\varepsilon,gm}^2}{1 + \sigma_{\eta,gm}^2 / \sigma_{\varepsilon,gm}^2}$$
$$= \frac{Rf_{\varepsilon,pulse}^2 + \sigma_{\eta,pulse}^2 / \sigma_{\varepsilon,gm}^2}{1 + \sigma_{\eta,gm}^2 / \sigma_{\varepsilon,gm}^2} = \frac{Rf_{\varepsilon,pulse}^2 + \sigma_{\eta,gm}^2 / \sigma_{\varepsilon,gm}^2}{1 + \sigma_{\eta,gm}^2 / \sigma_{\varepsilon,gm}^2} \quad (9)$$

$$\Rightarrow Rf_{\varepsilon,pulse} = \sqrt{(1 + \sigma_{\eta,gm}^2 / \sigma_{\varepsilon,gm}^2) \cdot Rf^2 - \sigma_{\eta,gm}^2 / \sigma_{\varepsilon,gm}^2} \quad (10)$$

The spatial correlation expression, $\rho_{\eta,gm}$, ([30, 40]) in Equation (11) can be used together with Equation (10) to express $Rf_{\varepsilon,\ pulse}$ as given in Equation (12).

$$\rho_{\eta,gm} = \sigma_{\eta,gm}^2 / (\sigma_{\varepsilon,gm}^2 + \sigma_{\eta,gm}^2) \quad (11)$$

$$Rf_{\varepsilon,pulse} = \sqrt{(Rf^2 - \rho_{\eta,gm}) / (1 - \rho_{\eta,gm})} \quad (12)$$

2.2 Development of hazard curves from MC-based MSRFs approach

We generate a suite of synthetic earthquake catalogs for a given fault located in the area of interest. The synthetic catalogs are based on a specific earthquake recurrence model that represents the temporal distribution of seismic activity in the considered fault for a certain catalog period. In essence, simulating a suite of synthetic earthquake catalogs having magnitude frequency distributions similar to the one dictated by the earthquake recurrence model and covering a long time span sufficiently addresses the low annual exceedance rates of earthquakes originating from the considered fault. This approach has been used by Musson [28] and Assatourias and Atkinson [29] in MC-based PSHA. Musson [28] indicated that a suite of 1000 synthetic catalogs, each spanning a 100-year time interval (i.e., a total duration of 100,000 years) would yield reliable estimates of GMIMs for annual exceedance rates of 10^{-3}. When the total catalog duration is extended to 1,000,000 years (i.e., 10000 synthetic catalog, each covering 100-year period), the accurate annual exceedance rates for GMIMs become 10^{-4}. Similar findings are also published by Assatourias and Atkinson [29] as well as Crowley and Bommer [26]. The latter paper considers all stochastic events in a single earthquake catalog with a very long time interval.

Our synthetic catalog simulations assume Poissonian process for earthquake occurrence. The earthquakes generated in each artificial catalog are assumed to occur randomly on the fault with a uniform distribution along the fault strike and within the seismogenic depth. For each scenario event in the artificial earthquake catalogs, we implement MSRFs approach to sample spatially correlated intra-event residuals at coarse- and fine-scale levels. The intra-event residuals are sampled at the centers of coarse-scale and fine-scale cells and consider the near-fault directivity effects depending on the relative location of the site (centroid of the cell) with respect to fault geometry. We obtain the total residual at each cell by considering the contribution of inter-event residual specific to the scenario event. The inter-event residuals are computed from the inter-event standard deviation of the GMPE used in the computations. They are sampled as normal varieties in our procedure. The logarithmic mean (median) predictions of GMIMs that are computed at the centers of coarse-scale and fine-scale cells are superposed with the total residuals to obtain the spatially correlated GMIM distribution within the entire random field. As in the case of intra-event residual sampling, the median GMIM predictions are modified for near-fault directivity effects depending on the center point of the cell and fault locations at coarse- and fine-scale levels.

The procedure described in the above paragraph is itemized in the following steps.

1. Define the area of interest together with the fault segment that affects the seismicity in the entire area. Subdivide the area into coarse-scale and fine-scale cells. The decision on the cell resolution (size) depends on many factors as MSRFs approach sample the GMIMs at the centroids of the cells. The clustering of geographically distributed portfolio and precision required to address the near-fault directivity effects are among the important factors that affect the cell size.
2. Chose a GMPE that is suitable for the tectonic environment as well as the seismicity in the area of interest. Equation (13) shows the essential components of a GMPE that are of relevance to our discussions.

$$\ln\left(GMIM_{i,j}\right) = f\left(M_i, R_{i,j}, \boldsymbol{\theta}\right) + \eta_i + \varepsilon_{i,j}; \qquad i = 1, \ldots . m,\ j = 1, \ldots n \tag{13}$$

The first term on the left-hand-side predicts the logarithmic mean of the $GMIM_{i,j}$ of interest for the *ith* earthquake and *jth* site (designated as $\mu_{lnGMIM,gm}$ in the previous discussions). M_i and $R_{i,j}$ are the magnitude and source-to-site distance terms of the *ith* earthquake and the *jth* site (centroid of the cell). The vector $\boldsymbol{\theta}$ contains other seismological estimator parameters to define, for example, site conditions at the *jth* site and style-of-faulting specific to the *ith* earthquake. The random varieties η_i and $\varepsilon_{i,j}$ represent the inter-event and intra-event variability in the predicted $GMIM_{i,j}$, respectively. They are normally distributed with inter-event ($\sigma_{\eta,gm}$) and intra-event ($\sigma_{\varepsilon,gm}$) standard deviations. Note that *m* and *n* in Equation (13), represent the total number of simulations and sites (cells) at coarse- and fine-scale levels, respectively. The total number of simulations is related to the number of earthquakes in the artificially generated earthquake catalogs.

3. Generate a suite of earthquake catalogs by following the properties of earthquake recurrence specific to the fault. The number of earthquake catalogs should be sufficient enough to consider the occurrence of rare events (low annual exceedance rates) for proper temporal distribution of earthquakes. Currently, the spatial distribution of earthquakes is defined by the uniformly distributed rupture planes and the hypocentral location of each earthquake is assumed to be at the center of the ruptured surface. The multi-segment or bending ruptures are disregarded in the implementation of the proposed approach.
4. For scenario event *i*, sample spatially correlated $\varepsilon_{i,j}$ using MSRFs approach. Make necessary calibrations for near-fault directivity effects at coarse-scale and fine-scale levels whenever necessary.
5. For scenario event *i*, compute the logarithmic mean of $GMIM_{i,j}$ ($\mu_{lnGMIM,gm}$) at coarse-scale and fine-scale levels. Make necessary calibrations for near-fault directivity effects (i.e., modify $GMIM_{i,j}$ either for $\mu_{lnGMIM,pulse}$ or $\mu_{lnGMIM,nonpulse}$) depending on the location of the centroid of the cell with respect to the fault, T_p and spectral period (T) of $GMIM_{i,j}$.
6. For scenario event *i*, compute η_i.
7. Combine the spatially correlated $\varepsilon_{i,j}$, $GMIM_{i,j}$ and η_i using Equation (13). The product is the spatially correlated $GMIM_{i,j}$ in the logarithmic domain at coarse- and fine-scale levels.
8. Repeat steps 4 to 7 for the simulated suite of earthquake catalogs and compute the hazard curves for the cells at coarse- and fine-scale levels from Equation (14).

$$\lambda_j(GMIM \geq GMIM_0) = \frac{total\ number\ of\ GMIM \geq GMIM_0\ at\ cell\ j}{total\ number\ of\ simulated\ earthquake\ catalogs \times\ catalog\ period} \quad (14)$$

In Equation (14), $\lambda_j(GMIM \geq GMIM_0)$ is the mean annual rate of GMIM of interest exceeding a threshold level $GMIM_0$ for cell *j*. Computation of $\lambda_j(GMIM \geq GMIM_0)$ for a range of $GMIM_0$ will yield the hazard curve at cell *j*. We note that the computation of hazard curves by MC-based MSRFs approach is described by considering a single fault source. If the area of interest is exposed to *k* multiple faults, this procedure is repeated for the other faults. The mean annul exceedance rates computed from all sources are then summed up to obtain the final mean annual exceedance rate at cell *j*.

$$\lambda_j(GMIM \geq GMIM_0) = \sum_{l=1}^{k} \lambda_{l,j}(GMIM \geq GMIM_0) \quad (15)$$

The concept introduced by Equation (15) can form the basis of MC-based hazard for areal sources. The uncertainty in the location and orientation of faults in areal sources can be represented by a set of virtual fault ruptures at which MC-based simulations can be repeated

for each selected orientation of the virtual fault ruptures. The total mean annual exceedance is computed at each cell by summing the contribution of hazard from each fictitious rupture.

2.3 Computation of conditional hazard

The discussions in the previous sections describe the theory and implementation of MC-based MSRFs approach for the seismic hazard assessment of a single GMIM. The conditional seismic hazard assessment, however, is sometimes more critical for geographically distributed structural portfolio and infrastructures because the seismic performance of some of their components require the consideration of multiple GMIMs. The conditional hazard assesses the exceedance rate of the secondary GMIMs conditioned on the occurrence of primary GMIM. The secondary GMIMs can be either single or multiple. In case there are multiple secondary GMIMs, they are called as first-secondary GMIM, second-secondary GMIM and so forth. The primary and secondary GMIMs are related to each other by cross-correlation coefficients, $\rho_{IMi,IMj}$ (e.g., [7, 12, 13]).

The conventional conditional hazard assessment cross-correlates each secondary GMIM with the primary GMIM to compute the conditional exceedance rate of the secondary GMIM [24]. The proposed procedure in this paper establishes a different structure: each secondary GMIM is cross-correlated with the primary and previously generated secondary GMIMs for the conditional exceedance rate of the secondary GMIMs. This way the interdependence of primary and secondary GMIMs is more realistically mapped on to the conditional exceedance rates. The procedure does not change for the primary GMIM. We generate the spatially correlated intra-event residuals and sum them up with the independently sampled inter-event residuals to obtain the total residual distribution at coarse- and fine-scale levels for the entire earthquake scenarios of the simulated earthquake catalogs. The total residual sampling of secondary GMIMs is based on the total residual distribution of the primary GMIM and they are generated via sequential conditional simulation. The total residuals of the primary and secondary GMIMs have joint multivariate normal distribution as described in Equations (16) and (17).

$$\begin{bmatrix} Z_{IMn} \\ \boldsymbol{Z}_{IMp} \end{bmatrix} \sim N(\boldsymbol{\mu}, \boldsymbol{\Sigma}) = N\left(\begin{bmatrix} 0 \\ \mathbf{0} \end{bmatrix}, \begin{bmatrix} \sigma_{IMn}^2 & \boldsymbol{\Sigma}_{IMnp} \\ \boldsymbol{\Sigma}_{IMpn} & \boldsymbol{\Sigma}_{IMpp} \end{bmatrix} \right) \tag{16}$$

$$\mathrm{COV}\left[Z_{IMi}, Z_{IMj} \right] \sim \rho_{Z_{IMi}, Z_{IMj}} \cdot \sigma_{Z_{IMi}} \cdot \sigma_{Z_{IMj}} \tag{17}$$

Equations (16) and (17) have a format similar to Equations (6) and (8), respectively. Z_{IMn} refers to the next generated total residual of secondary GMIM whereas $\boldsymbol{Z_{IMp}}$ is the vector of previously generated primary and secondary GMIMs. In a similar manner, σ_{IMn} is the total standard deviation of the next generated secondary GMIM and $\sum_{\boldsymbol{IMnp}}$ as well as $\sum_{\boldsymbol{IMpn}}$ are the covariance vectors of the previous and next GMIMs, respectively. The covariance matrix of the previously generated GMIMs is designated as $\sum_{\boldsymbol{IMpp}}$. Note that the covariance terms in Equation (16) contain the previously generated primary and secondary GMIMs as the proposed approach accounts for the interdependency between these varieties. The covariance relationship to be used between the secondary and primary, primary and primary as well as secondary and secondary GMIMs are given in Equation (17). In this expression, $\rho_{IMi,IMj}$ is the cross-correlation coefficient between GMIM_i and GMIM_j where they can be primary and secondary, both secondary or both primary GMIMs. σ_{ZIMi} and σ_{ZIMi} refer to the corresponding total standard deviations. As explained in the previous sections the standard deviation information comes

from the GMPE used in the overall process. The total residual distribution can further be expressed as a univariate normal distribution for the next generated GMIM as given in Equation 18, which is analogous to Equation (7) used in the inter-event residual sampling of primary GMIM.

$$\left[Z_{IMn} \mid \boldsymbol{Z}_{IMp} = \boldsymbol{z} \right] \sim N\left(\boldsymbol{\Sigma}_{IMnp} \cdot \boldsymbol{\Sigma}_{IMpp}^{-1} \cdot \boldsymbol{z}, \sigma_{IMn}{}^{2} - \boldsymbol{\Sigma}_{IMnp} \cdot \boldsymbol{\Sigma}_{IMpp}^{-1} \cdot \boldsymbol{\Sigma}_{IMpn} \right) \tag{18}$$

In Equation (18) $\boldsymbol{Z_{IMp}}$ is the total residual realizations of the previous GMIMs. Note that we describe the proposed procedure to sample cross-correlated total residuals. If the considered GMPE provides information about the cross-correlation models of intra- and inter-event residuals separately, it can be modified to sample the cross-correlated intra- and inter-event residuals simultaneously to obtain the hazard rate of secondary GMIMs conditioned on the primary GMIM.

In essence, our procedure for conditional hazard assessment uses the previously generated primary GMIM to sample the total residuals of secondary GMIMs. If there is a second-secondary GMIM, its total residuals are sampled by the cross-correlations of primary, first-secondary and second-secondary GMIMs. This process continues for the entire set of secondary GMIMs. The conditional hazard of each secondary GMIM is then developed by following the conventional approach given in Equation (14). If there is one secondary GMIM, the normal distribution of total residuals of the secondary GMIM will have the following mean ($\mu_{IM2|IM1}$) and standard deviation ($\sigma_{IM2|IM1}$):

$$\mu_{IM\,2|IM\,1} = \rho_{IM\,1,IM\,2}\sigma_{IM\,2}\frac{\varepsilon}{\sigma_{IM\,1}} \tag{19}$$

$$\sigma_{IM\,2|IM\,1} = \sigma_{IM\,2}\sqrt{1-\rho_{IM\,1,IM\,2}^{2}} \tag{20}$$

In Equation (19), ε is the previously sampled total residual of primary GMIM and $\rho_{IM1,IM2}$ is the cross-correlation coefficient between the primary and secondary GMIMs. Figure 5 illustrates this specific case to develop the hazard curve of the secondary GMIM conditioned on the primary GMIM for the centroid of each cell. We note that the proposed procedure assumes that the correlation distances of the secondary IMs are the same as that of primary IM. Therefore, it is suggested to choose the primary IM as the one with larger correlation length with respect to the correlation distances of secondary IMs [15, 37].

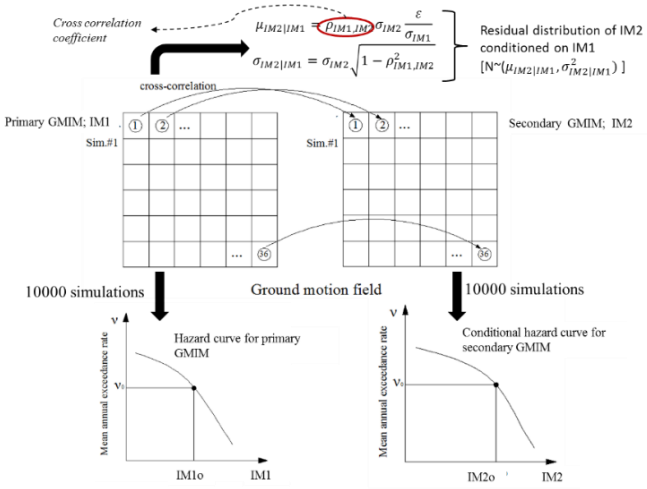

Figure 5. Graphical illustration of conditional hazard assessment for one secondary GMIM

4. CASE STUDIES

We present several case studies to show the implementation and implications of the theory discussed in this article. The case studies intend to emphasize the flexibility and robustness of MC-based simulations for probabilistic hazard assessment of dynamic GMIMs. We used our own Matlab^{TM} codes while running the case studies. We validated our codes by comparisons with the results of open-source seismic hazard software, OpenQuake (http://www.globalquakemodel.org/openquake). The details of case studies are given in the following subsections. The seismic sources are represented as fault segments in the case studies although they could also be chosen as area sources with some modifications in the procedures discussed in Section 2.

4.1 Case studies concerning dynamic GMIMs

Figure 6 shows the results of the validation of our codes for a fictitious 90° dipping strike-slip fault segment of length 85 km. We consider pure-characteristic earthquake recurrence model with characteristic magnitudes ranging between M_w 7 and M_w 7.5 (uniformly distributed probabilities of occurrence between M_w 7 and M_w 7.5). The annual slip rate is assumed as 15 mm/year for the fictitious fault. We ran 10,000 simulations with a 100-year catalog period (total catalog period is 1,000,000 years) to obtain reliable hazard results for mean annual exceedance rates of about10^{-4} [28]. We used Akkar et al. [41, 42] GMPE to characterize the ground-motion amplitudes in the hazard analyses. The same fictitious scenario is modeled in OpenQuake [43] using the conventional PSHA [22, 44] to validate the reliability of our computations. Our results and the results from OpenQuake are compared for PGA hazard curves at the randomly selected rock sites (see upper right corner in Figure 6 for the relative locations of sites with respect to the fault). The results computed by our codes agree well with OpenQuake for mean annual exceedance rates up to 10^{-4}. We repeated similar verification studies for different dynamic GMIMs and sites with locations different than those given in this exercise. These comparisons advocate the reliability of our codes to discuss how different levels of complexity (directivity, spatial correlation, conditional hazard etc.) are treated by MC-based approaches for probabilistic hazard assessment.

Similar to the above validation example, the following case studies use a 90° dipping strike-slip fault although our codes can run hazard analyses for other styles of faulting. The fault length is 85 km and its seismogenic depth is taken as 15 km. The fictitious fault is assumed to have a slip rate of 15 mm/year producing characteristic earthquakes of M_w 7.0 to M_w 7.5. In all case studies, we used a 100-year catalog period and ran 10,000 simulations that results in a total catalog interval of 1,000,000 years. The spatial correlation model of Jayaram and Baker [4] is utilized for the interdependency of dynamic GMIMs at closely spaced sites. The Akkar et al. [41, 42] GMPE and the Akkar et al. [12, 13] cross-correlation coefficients are used for ground-motion characterization and conditional hazard computations, respectively. These two studies use the same strong-motion database to develop the ground-motion predictive model and the correlations between the spectral ordinates. The site condition is fixed in all case studies and is represented by V_{S30} = 720 m/s. The size of coarse cells is chosen as 0.1°×0.1° and they are refined by 4×4 fine scale cells at sites closer to the fault.

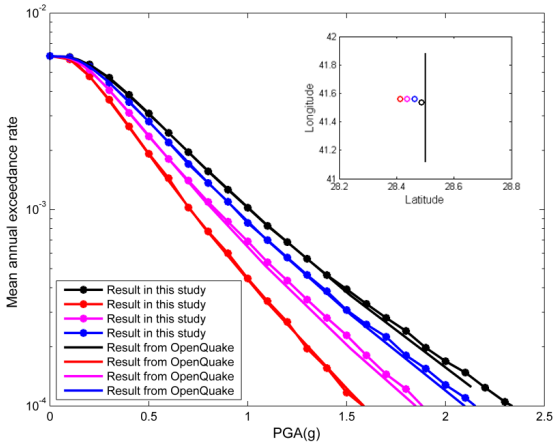

Figure 6. Comparisons of OpenQuake PGA hazard curves with those computed from in-house Matlab™ codes developed for running MC-based MSRFs technique.-The site conditions are characterized by V_{S30} = 720m/s

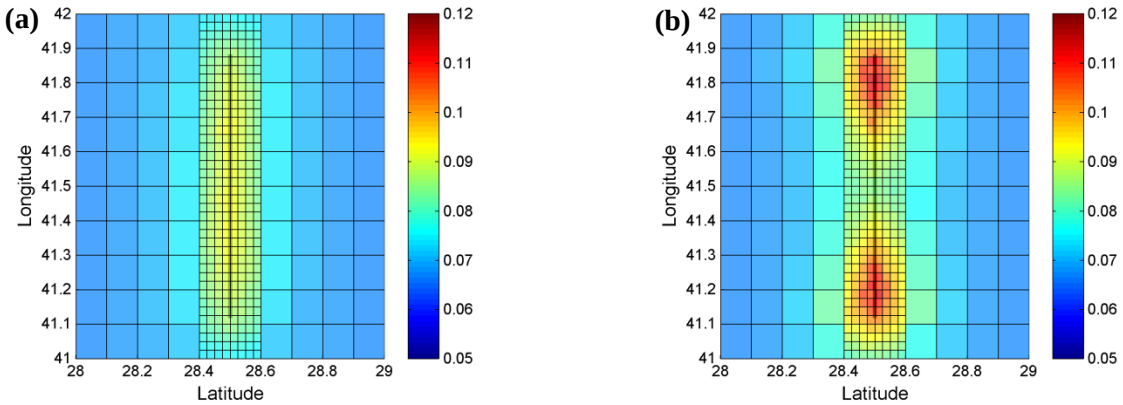

Figure 7. Distribution of S_a(3s) amplitudes for 475-year return period (a) without and (b) with near-fault directivity effects. The fault segment is shown as a dark solid line on the plots.

Figure 7 shows the influence of near-fault directivity effects on the distribution of 475-year return period spectral acceleration at T = 3.0s [S_a(3s)]. Figure 7a displays the distribution of S_a(3s) when the near-fault directivity effects are disregarded in the hazard assessment. The spectral amplitude distribution follows a uniform pattern attaining its maximum in the vicinity of entire fault length and decreases gradually towards distant sites from the fault. The spectral amplitude distribution in Figure 7b considers the directivity effects for the same case. The maximum spectral amplitudes are observed at the ends of the fault segment. They are approximately 20% to 25% larger with respect to those that disregard the forward directivity. The spectral amplitudes in the middle portion of the fault segment are smaller in Figure 7b when compared to the corresponding spectral values in Figure 7a. These observations emphasize the importance of site location with respect to fault orientation when near-fault effects are mapped on to the hazard. The spectral amplitude comparisons between Figures 9a and 9b suggest the insignificance of directivity effects for distances greater than 10 km from the fault segment. We note that these observations are confined to a specific source configuration and return period (i.e., 475-year return period). The influence of forward

directivity on spectral amplitudes increases for larger return periods and higher seismic activity (i.e., larger slip rates).

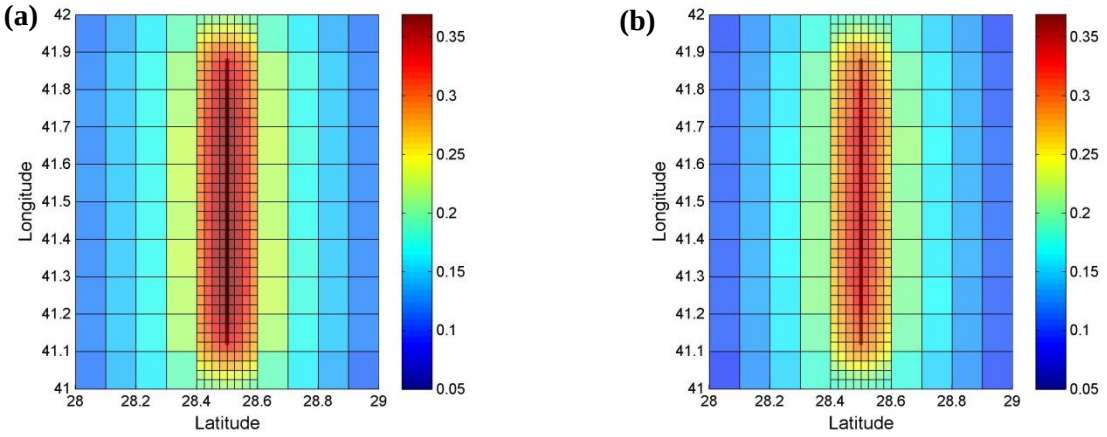

Figure 8. Distribution of (a) S_a(1.0s) and S_a(1.0s)|S_a(3.0s) for 475-year return period. The fault segment is shown as dark solid line on the plots

The left and right panels in Figure 8 display the significance of conditional hazard on dynamic GMIMs and how it is accounted for by MC-based MSRFs approach. The plots show the distributions of S_a(1.0s) (Figure 8.a) and S_a(1.0)|S_a(3s) (Figure 8.b) for 475-year return period. The distribution of S_a(1.0s) conditioned on S_a(3.0s) displays 10% to 15% lower spectral amplitudes with respect to the distribution of S_a(1.0s) at sites closer to the fault. Such spectral differences can be important for the design or performance assessment of high-rise buildings under the influence of higher mode effects. For example, S_a(1.0s)|S_a(3.0s) distribution could be important for a tall building of 3.0s fundamental period (T_1) whose second mode (T_2 = 1.0s) has a considerable effect on its dynamic response. To this end, the approach presented in this article would yield useful information for the spatial variation of such vector GMIMs for the probabilistic risk and loss assessment of geographically distributed building inventories (e.g., [37]).

Figure 9 illustrates a more sophisticated case study in which the significance of spatial correlation (SC) and near-fault forward directivity (NF) effects is discussed for three spectral periods at three different locations relative to the fault segment (Figure 9.a). We consider a pair of sites at each location for spatial correlation effects. The pairs are closely spaced at locations 2 and 3 whereas the separation distance between the sites at location 1 is larger. The chosen spectral ordinates represent very short-period (PGA-T = 0.0s; Figure 9.b), intermediate-period (T = 0.5s; Figure 9.c) and long-period (T = 3.0s; Figure 9.d) ground-motion demands. The comparative plots in Figure 9 suggest that consideration of spatial correlation has negligible influence at location 1 due to large separation distance between the sites. This observation particularly holds for very short period (Figure 9.b) and intermediate period (Figure 9.c) spectral ordinates. For longer periods (Figure 9.d), disregarding SC effects at location 1 yields slightly lower spectral amplitudes with respect to the case when this effect is considered. We note that the NF effects are insignificant for PGA as well as for S_a(0.5s) at all sites because they become effective after T = 0.6s in the Shahi and Baker [18] model. Disregarding spatial correlation has more pronounced effects for the 2nd and 3rd locations as the sites are closely spaced at these locations. Seismic hazard assessment that overlooks SC always underestimates spectral amplitudes that increases with increasing annual exceedance rate and spectral period. The consideration of NF effects has different implications for the three locations considered in

this study for periods shifting to longer spectral period bands (Figure 9.c). The NF effects are immaterial at the first location as it is far from the fault segment (~ 25 km). Consideration of NF effects amplifies S_a(3.0s) at location 3 and de-amplifies it at location 2. As discussed in Figure 7, the near-fault forward directivity effects are pronounced at the ends of the fault segments (e.g., location 3) and become minimum at the mid segment of the fault (e.g., location 2).

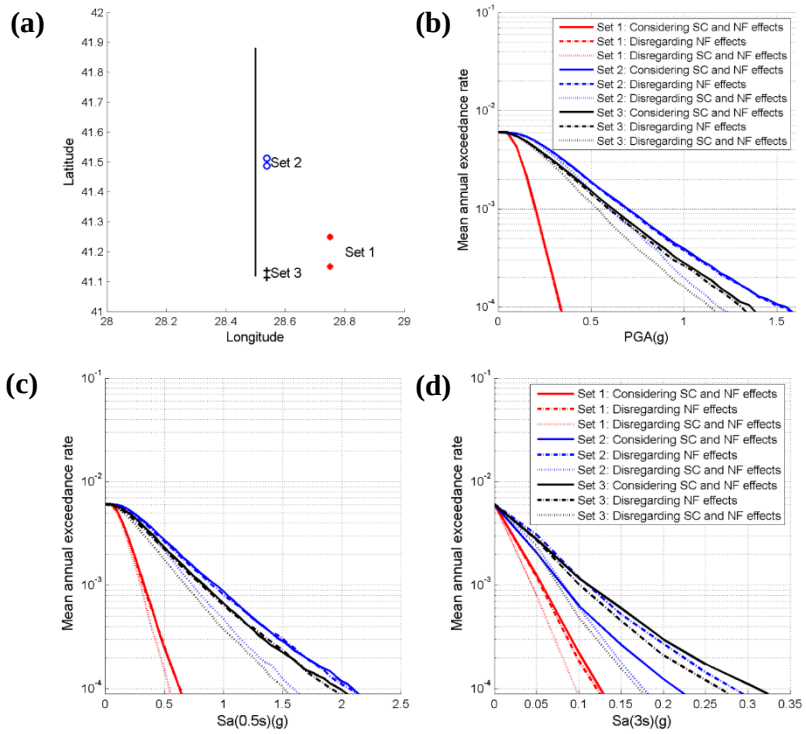

Figure 9. Effect of spatial correlation (SC) and near-fault forward directivity (NF) effects at three different locations for three spectral periods (a) Plan-view of locations, sites and the fault segment, (b) joint hazard curves for PGA, (c) joint hazard curves for S_a(0.5s), and (d) joint hazard curves for S_a(3s)

5. CONCLUSION

We present the implementation of MC-based simulation techniques for probabilistic hazard assessment of dynamic GMIMs. The MC-based simulations are incorporated with multi-scale random fields (MSRFs) approach to account for the spatial correlation, near-fault forward directivity and conditional hazard (cross-correlation) in the variation of dynamic intensity measures. Consideration of all these factors via conventional (integral) PSHA can be computationally challenging. The multi-scale random fields also provide flexibility for instant modification of intra-event aleatory variability whenever it is necessary (e.g., near-fault forward directivity effect).

The theoretical aspects presented in the paper are validated by a limited number of case studies. These exercises suggest the reliability of our MC-based probabilistic hazard results when compared to their counterparts obtained from conventional PSHA. Other case studies showing the influence of near-fault directivity, spatial correlation and conditional hazard advocate that

each one of these complexities can effectively modify the hazard upon their deliberate implementation. In essence the MC-based techniques discussed in the paper provide flexibility to observe the effects of such specific features on hazard without running complicated probabilistic hazard integrals.

ACKNOWLEDGEMENTS

The studies presented in this paper are the products of the STREST project (Harmonized approach to stress tests for critical infrastructures against natural hazards) that is funded by the European Union's Seventh Framework Programme under grant agreement no. 603389. The computer codes developed within the framework of the paper will be public-open via project web site at the end of the project. Positive and constructive comments of Prof. Julian Bommer and Dr. Graeme Weatherill increased the quality of discussions in the paper.

REFERENCES

1. Boore DM, Gibbs JF, Joyner WB, Tinsley JC, Ponti DJ. Estimated ground motion from the 1994 Northridge, California, earthquake at the site of the Interstate 10 and La Cienega Boulevard bridge collapse, West Los Angeles, California. *Bulletin of the Seismological Society of America* 2003; **93**(6): 2737–2751.
2. Wang M, Takada T. Macrospatial Correlation Model of Seismic Ground Motions. *Earthquake Spectra* 2005; **21**(4):1137–1156.
3. Goda K, Hong HP. Spatial Correlation of Peak Ground Motions and Response Spectra. *Bulletin of the Seismological Society of America* 2008; **98**(1): 354–365.
4. Jayaram N, Baker JW. Correlation model of spatially distributed ground motion intensities. *Earthquake Engineering & Structural Dynamics* 2009; **38**(15): 1687–1708.
5. Esposito S, Iervolino I. PGA and PGV spatial correlation models based on European multievent datasets. *Bulletin of the Seismological Society of America* 2011; 101(5): 2532–2541.
6. Goda K, Atkinson GM. Probabilistic characterization of spatially correlated response spectra for earthquakes in Japan. *Bulletin of the Seismological Society of America* 2009; **99**(5): 3003-3020.
7. Baker J, Jayaram N. Correlation of Spectral Acceleration Values from NGA Ground Motion Models. *Earthquake Spectra* 2008; **24**(1): 299–317.
8. Bradley BA. Empirical correlation of PGA, spectral accelerations and spectrum intensities from active shallow crustal earthquakes. *Earthquake Engineering and Structural Dynamics* 2011; **40**(15):1707–1721.
9. Bradley BA. Empirical correlations between cumulative absolute velocity and amplitude-based ground motion intensity measures. *Earthquake Spectra* 2012; **28**(1): 17–35.
10. Bradley BA. Empirical Correlations between Peak Ground Velocity and Spectrum-Based Intensity Measures. *Earthquake Spectra* 2012; **28**(1): 37–54.
11. Cimellaro GP. Correlation in spectral accelerations for earthquakes in Europe. *Earthquake Engineering & Structural Dynamics* 2013; **42**(4): 623-633.

12. Akkar S, Sandıkkaya MA, Ay BÖ. Compatible ground-motion prediction equations for damping scaling factors and vertical-to-horizontal spectral amplitude ratios for the broader Europe region. *Bulletin of Earthquake Engineering* 2014; **12**(1): 517-547
13. Akkar S, Sandikkaya MA, Ay BÖ. Erratum to: Compatible ground-motion prediction equations for damping scaling factors and vertical-to-horizontal spectral amplitude ratios for the broader Europe region. *Bulletin of Earthquake Engineering* 2014; **12**(3): 1429-1430.
14. Cheng Y, Lucchini A, Mollaioli F. Correlation of elastic input energy equivalent velocity spectral values for ground motions. *Earthquakes and Structures* 2015; **8**(5): 957-976.
15. Loth C, Baker JW. A spatial cross-correlation model of spectral accelerations at multiple periods. *Earthquake Engineering & Structural Dynamics* 2013; **42**(3): 397–417.
16. Somerville PG. Magnitude scaling of the near fault rupture directivity pulse. *Physics of the Earth and Planetary Interiors* 2003; **137**(1) 201–212.
17. Tothong P, Cornell CA, Baker JW. Explicit-directivity-pulse inclusion in probabilistic seismic hazard analysis. *Earthquake Spectra* 2007; **23**(4): 867–891.
18. Shahi S, Baker JW. An empirically calibrated framework for including the effects of near-fault directivity in probabilistic seismic hazard analysis. *Bulletin of the Seismological Society of America* 2011; **101**(2): 742–755.
19. Bayless J, Somerville P. *Bayless-Somerville Directivity Model*. Report PEER 2013/09. Berkeley, Calif.: Pacific Earthquake Engineering Research Center, University of California, 2013.
20. Chiou BSJ, Spudich P. *The Chiou and Spudich Directivity Predictor DPP*. Report PEER 2013/09. Berkeley, Calif.: Pacific Earthquake Engineering Research Center, University of California, 2013.
21. Rowshandel B. *Rowshandel's NGA-West2 directivity model.* Report PEER Report 2013/09, Berkeley, Calif.: Pacific Earthquake Engineering Research Center, University of California, 2013.
22. Cornell CA. Engineering seismic risk analysis. Bulletin of the Seismological Society of America 1968; 58(5): 1583-1606.
23. Stepp JC, Wong I, Whitney J, Quittmeyer R, Abrahamson N, Toro G, Youngs R, Coppersmith K, Savy J, Sullivan T, Yucca Mountain PSHA Project Members. Probabilistic seismic hazard analyses for ground motions and fault displacement at Yucca Mountain, Nevada. *Earthquake Spectra* 2001; **17**(1): 113–150.
24. Iervolino I, Giorgio M, Galasso C and Manfredi G. Conditional hazard maps for secondary intensity measures. *Bulletin of the Seismological Society of America* 2010; **100**(6): 3312–3319.
25. Chioccarelli E, Esposito S, Iervolino I. Implementing conditional hazard for earthquake engineering practice: the Italian example. In *Proceedings of the 15th World Conference on Earthquake Engineering*, Lisbon, Portugal, 2012.
26. Crowley H, Bommer JJ. Modelling seismic hazard in earthquake loss models with spatially distributed exposure. *Bulletin of Earthquake Engineering* 2006; **4**(3): 249-273.
27. Musson RMW. Determination of design earthquakes in seismic hazard analysis through Monte Carlo simulation. *Journal of Earthquake Engineering* 1999; **3**(4): 463-474.
28. Musson RMW. The use of Monte Carlo simulations for seismic hazard assessment in the UK. *Annali Di Geofisica* 2000; **43**(1): 1–9
29. Assatourians K, Atkinson GM. EqHaz: An open ‐ source probabilistic seismic ‐ hazard code based on the Monte Carlo simulation approach. *Seismological Research Letters* 2013; **84**(3): 516-524.

30. Sokolov V, Wenzel F. Influence of ground-motion correlation on probabilistic assessments of seismic hazard and loss: sensitivity analysis. *Bulletin of Earthquake Engineering* 2011; **9**(5): 1339–1360.
31. Sokolov V, Wenzel F. Influence of spatial correlation of strong ground motion on uncertainty in earthquake loss estimation. *Earthquake Engineering & Structural Dynamics* 2011; **40**(9): 993–1009.
32. Atkinson GM, Goda K. Seismic risk analysis and management of civil infrastructure systems: an overview, Chapter 1. *Handbook of Seismic Risk Analysis and Management of Civil Infrastructure Systems*. Cambridge, UK: Woodhead Publishing Ltd, 2013.
33. Bal IE, Bommer JJ, Stafford PJ, Crowley H, Pinho R. The influence of geographical resolution of urban exposure data in an earthquake loss model for Istanbul. *Earthquake Spectra* 2010; **26**(3), 619–634.
34. Jayaram N, Baker JW. Efficient sampling and data reduction techniques for probabilistic seismic lifeline risk assessment. *Earthquake Engineering & Structural Dynamics* 2010; **39**(10):1109–1131
35. Wang Y, Au S, Fu Q. Seismic risk assessment and mitigation of water supply systems. *Earthquake Spectra* 2010; **26**(1): 257–74.
36. Esposito S, Iervolino I, d'Onofrio A, Santo A. Simulation-Based Seismic Risk Assessment of Gas Distribution Networks. *Computer-Aided Civil and Infrastructure Engineering* 2015; **30**(7): 508–523.
37. Weatherill G, Silva V, Crowley H, Bazzurro P. Exploring the impact of spatial correlations and uncertainties for portfolio analysis in probabilistic seismic loss estimation. *Bulletin of Earthquake Engineering* 2015; **13**(4): 957-981.
38. Chen Q, Seifried A, Andrade. JE, Baker JW. Characterization of random fields and their impact on the mechanics of geosystems at multiple scales. *International Journal for Numerical and Analytical Methods in Geomechanics* 2012; **36**(2):140–165.
39. Stafford PJ. Evaluation of structural performance in the immediate aftermath of an earthquake: a case study of the 2011 Christchurch earthquake. International Journal of Forensic Engineering 2012; **1**(1): 58–77.
40. Wesson RL, Perkins DM. Spatial correlation of probabilistic earthquake ground motion and loss. *Bulletin of the Seismological Society of America* 2001; **91**(6): 1498-1515.
41. Akkar S, Sandıkkaya MA, Bommer JJ. Empirical ground-motion models for point-and extended-source crustal earthquake scenarios in Europe and the Middle East. *Bulletin of Earthquake Engineering* 2014; **12**(1): 359–387.
42. Akkar S, Sandıkkaya MA, Bommer JJ. Erratum to: Empirical ground-motion models for point- and extended-source crustal earthquake scenarios in Europe and the Middle East. *Bulletin of Earthquake Engineering* 2014; **12**(1):389–390.
43. Pagani M, Monelli D, Weatherill G, Danciu L, Crowley H, Silva V. OpenQuake Engine: An Open Hazard (and Risk) Software for the Global Earthquake Model. *Seismological Research Letters* 2014; **85**(3):692-702.
44. McGuire RK. FORTRAN Computer Program for Seismic Risk Analysis, *USGS Open File Report 76-67*, 1976.

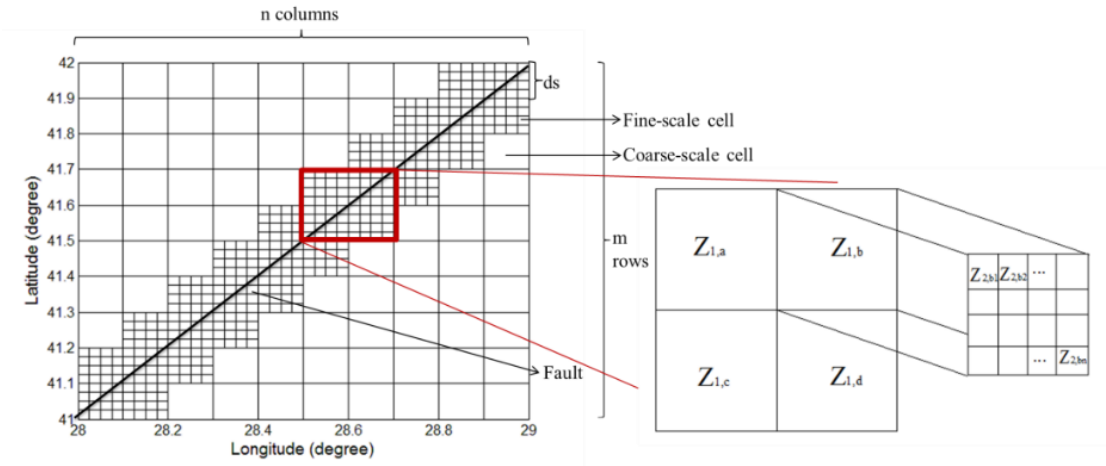

Figure 1. Graphical representation of coarse-scale and fine scale cells. The solid diagonal line is the fault. The area enclosing the fault segment is divided into *m*×*n* coarse-scale cells. Some of the coarse-scale cells are further refined into *ds*×*ds* fine scale cells. The right panel is the close-up view of 4 coarse scale cells located in the vicinity of the fault and, for illustration purposes, we show one of these coarse scale cells refined into 4×4 fine-scale cells

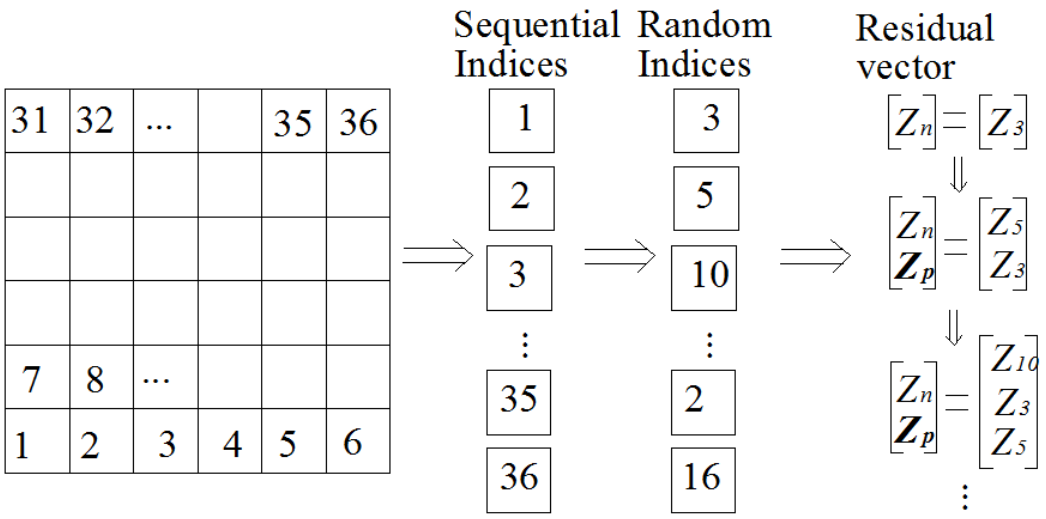

Figure 2. Illustrative example for intra-event residual sampling at coarse-scale level

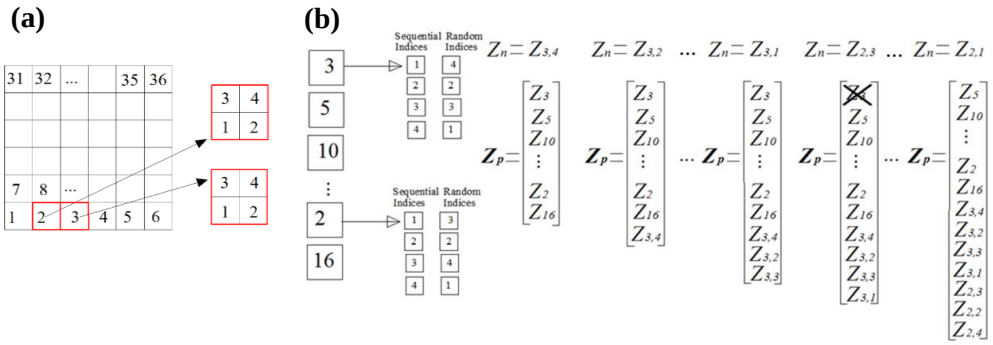

Figure 3. Generation of intra-event residuals for fine-scale cells: (a) pre-selected coarse-scale cells for refining into fine-scale cells (designated by red boxes) and numbering of fine-scale cells in these coarse-scale cells, (b) sequential conditional simulation process

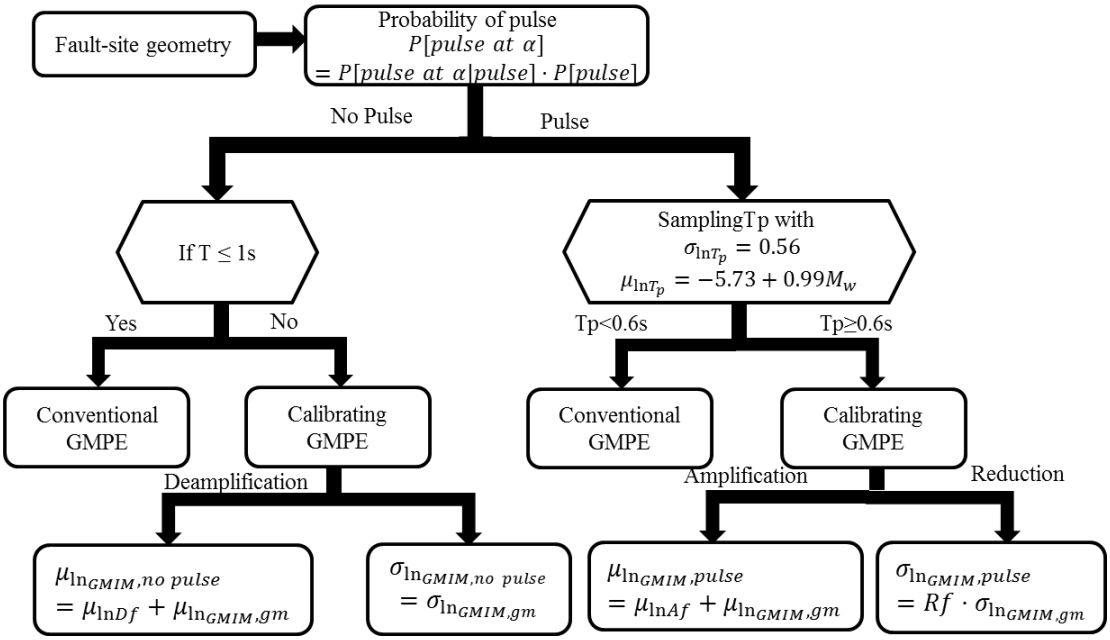

Figure 4. Algorithm for considering near-fault forward directivity effects on the spatially correlated GMIMs generated from MSRFs approach. $\mu_{lnGMIM,pulse}$ is the calibrated mean GMIM in logarithmic space due to pulse-like ground motions (forward directivity). μ_{lnAF} is the logarithmic calibration factor for forward directivity effects and $\mu_{lnGMIM,gm}$ is the mean GMIM in logarithmic space computed from conventional GMPE. In a similar manner, $\sigma_{lnGMIM,pulse}$ and $\sigma_{lnGMIM,gm}$ are the calibrated and original standard deviations of conventional GMPE, respectively. *Rf* is the calibration factor for standard deviation for forward directivity effects. For non-pulse case, $\mu_{lnGMIM,nonpulse}$ is the calibrated mean GMIM in logarithmic space due to non-pulse-like ground motions. μ_{lnAF} and $\sigma_{lnGMIM,nonpulse}$ are the logarithmic calibration factor and standard deviation of GMPE for backward directivity effects, respectively.

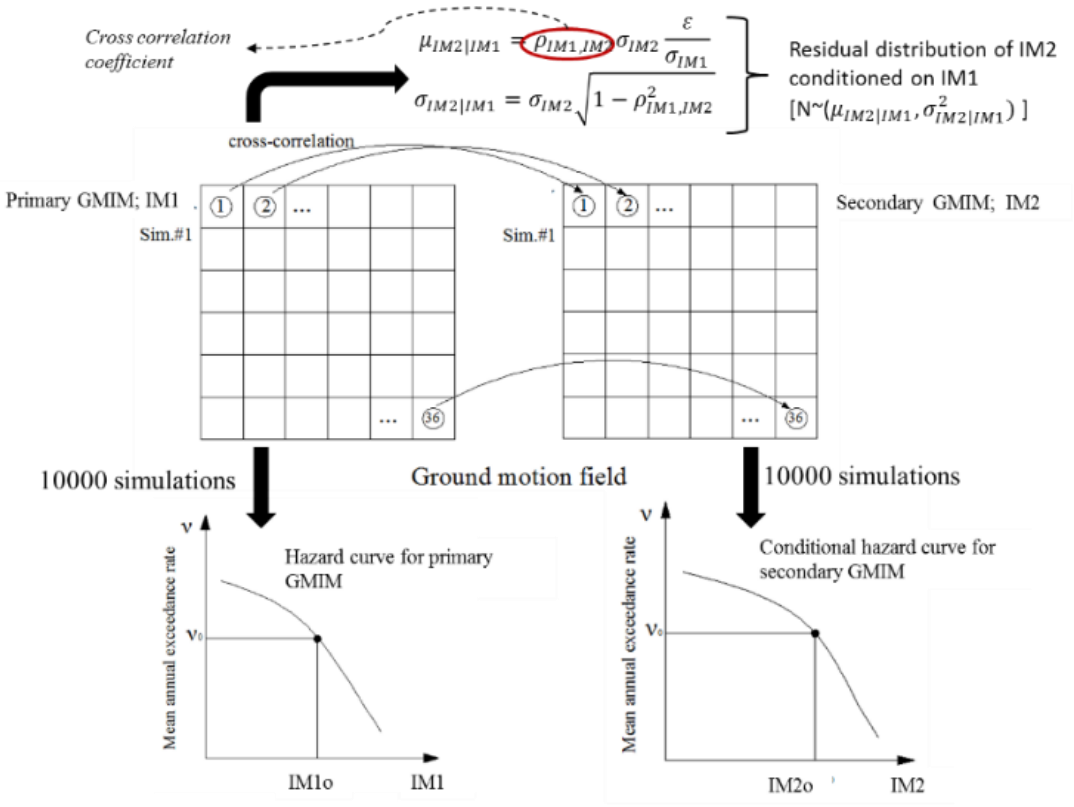

Figure 5. Graphical illustration of conditional hazard assessment for one secondary GMIM

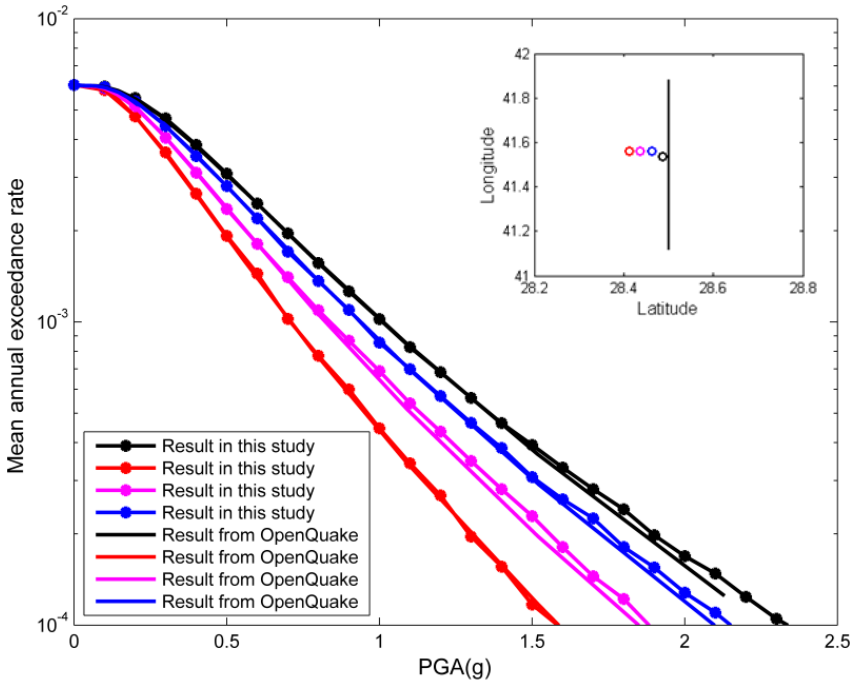

Figure 6. Comparisons of OpenQuake PGA hazard curves with those computed from in-house Matlab^{TM} codes developed for running MC-based MSRFs technique.-The site conditions are characterized by V_{S30} = 720m/s

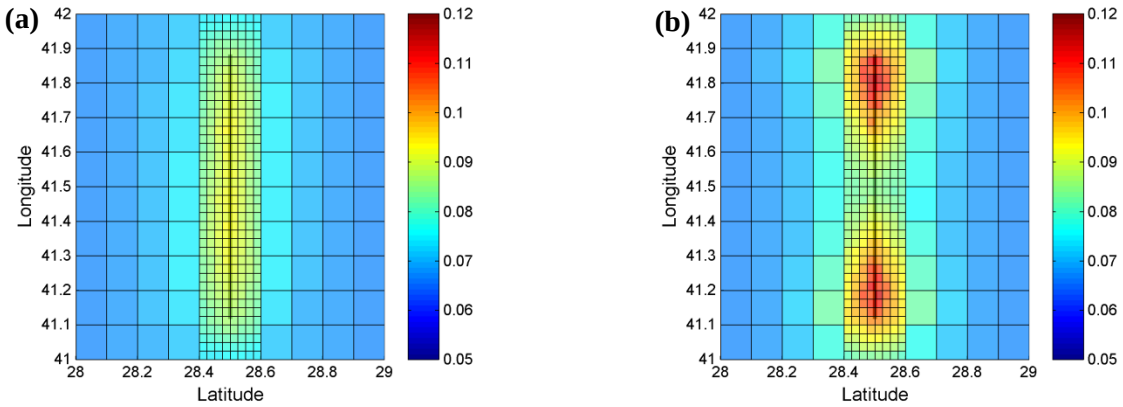

Figure 7. Distribution of S_a(3s) amplitudes for 475-year return period (a) without and (b) with near-fault directivity effects. The fault segment is shown as a dark solid line on the plots.

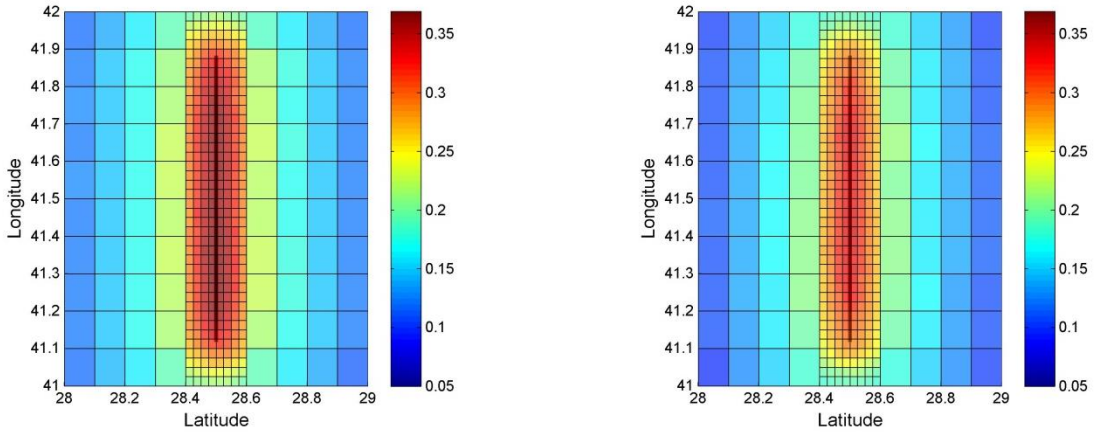

Figure 8. Distribution of (a) S_a(1.0s) and S_a(1.0s)|S_a(3.0s) for 475-year return period. The fault segment is shown as dark solid line on the plots

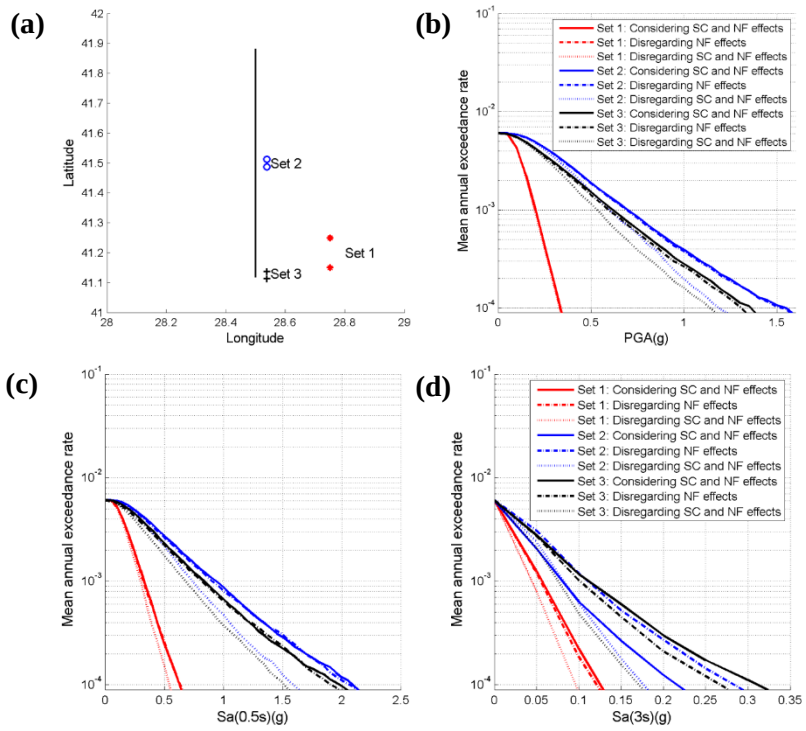

Figure 9. Effect of spatial correlation (SC) and near-fault forward directivity (NF) effects at three different locations for three spectral periods (a) Plan-view of locations, sites and the fault segment, (b) joint hazard curves for PGA, (c) joint hazard curves for S_a(0.5s), and (d) joint hazard curves for S_a(3s)